ISSN 2616-5872 Vol. 7, Issue 1: 23-36, DOI: 10.25236/AJEE.2025.070103

Study on the Impact of Atmospheric Compound Pollutants on Air Quality in China during Sandy and Dusty Weather: A Case Study of March 2021

Jiaqi Wang[1,2,a], Tianzhen Ju[1,2,b,*], Bingnan Li[3,c], Yaqun Cao[1,2,d], Jiachen Li[1,2,e]

[1]College of Geography and Environmental Sciences, Northwest Normal University, Lanzhou, China
[2]The Key Laboratory of Resource Environment and Sustainable Development of Oasis, Lanzhou, Gansu Province, China
[3]News and Mass Communication Department, Shaanxi Normal University, Xi'an, 710062, China
[a]2022223083@nwnu.edu.cn, [b]sandstorm608@163.com, [c]bingnanli@snnu.edu.cn,
[d]2022223101@nwnu.edu.cn, [e]20222113029@nwnu.edu.cn
[*]Corresponding author

Abstract: *Horizontal dynamic monitoring of the sand and dust weather process was conducted using ground-level $PM_{2.5}$ and PM_{10} data. The transport paths and potential sources of the sand and dust were analyzed through clustering of backward trajectories from the HYSPLIT model. Changes in the distribution of SO_2, NO_2, and O_3 during the sand and dust weather were examined using remotely sensed data. The results indicated that: (1) The significant impact of sand and dust storms on regional air pollution in 2021, from March 13 to April 21, both PM_{10} and $PM_{2.5}$ exhibited an overall west-to-east distribution change, with similar spatial and temporal patterns. PM_{10} showed the most pronounced changes, with the largest pollution range occurring on March 16, where the highest concentration reached 4943 μg/m³. The mean concentration increased by 127.1% compared to pre-sand and dust conditions. The maximum concentration peaked at 1155.70 μg/m³, representing a 190.4% increase from the initial dust levels. The daily average concentration rose from 46.34 μg/m³ on March 14 to 78.63 μg/m³, a 69.68% increase. The maximum UVAI pollution area was observed on March 15, with a peak value of 5.14 and an average value of 2.86, which is 1.9 times higher than pre-sand and dust conditions. (2) The different atmospheric components during dusty weather exhibited unique spatial and temporal evolution characteristics. The diffusion range of UVAI was largely consistent with the evolution of dust storms, with an influence range far exceeding that of PM_{10}. Its concentration maximum and mean values increased by approximately 189% and 64%, respectively, compared to pre-dust storm conditions. The response of NO_2 showed a noticeable lag, with concentrations exhibiting a distribution pattern of lower in the northwest and higher in the southeast. The peak concentration increased by 155% compared to pre-dust storm levels. The concentration of SO_2 demonstrated an overall decreasing trend, particularly in the early stages of the dust storm due to enhanced turbulence, with the maximum value decreasing by up to 94.6%. This change occurred earlier than that of PM_{10} and $PM_{2.5}$. O_3 responded to the dust storm with a lag, and the impact was geographically specific, with the average value showing little change and the maximum value increasing by approximately 32%.(3) The sand source of this dusty weather is complex, and the transmission path is primarily divided into three branches: the northwest route, the west route, and the north route. The primary sand sources for the first dust storm include Kazakhstan and Kyrgyzstan outside the country, as well as the Taklamakan and Gurbantunggu deserts within the country. The second dust storm was caused by Mongolian air masses carrying sand and dust from abroad, superimposed on sand and dust from the Maowusu Desert. The combination of overseas inputs and regional sand sources was crucial to the formation of widespread pollution in both dust storms.*

Keywords: *Dusty weather, air quality, spatial and temporal distribution, path analysis, pollution concentration*

1. Introduction

Dusty weather is a complex meteorological phenomenon with significant impacts on human health[1], ecology[2, 3], and regional and global climate change[4]. Research has demonstrated that dust particles not only pose direct threats to human life and health, such as causing respiratory and cardiovascular diseases[5], but also exacerbate air pollution through interactions with other aerosols[4, 6, 7]. Consequently,

ISSN 2616-5872 Vol. 7, Issue 1: 23-36, DOI: 10.25236/AJEE.2025.070103

the hazards and management of dusty weather remain a critical focus for both academics and policymakers worldwide.

Due to the unique geographic location and climatic conditions of China, sand sources are widely distributed both within and around the ountry, making it particularly susceptible to sand and dust storms in winter and spring[8]. To address these challenges, China has formulated and implemented the National Plan for Sand Control and Prevention (2021-2030), which sets out several goals, including the completion of 100 million mu of sandy land management by 2025 and 186 million mu by 2030. These initiatives provide policy support for sand and dust prevention and control, as well as environmental improvement, and also place higher scientific demands on sand and dust monitoring and traceability research.

In recent years, satellite remote sensing technology has played a crucial role in monitoring sand and dust weather due to its high precision, strong timeliness, and extensive coverage capabilities. Scholars both domestically and internationally have utilized satellite inversion products containing sand and dust discrimination information, such as aerosol optical thickness (AOD) and sand and dust indices from EOS/MODIS[9], infrared difference sand and dust indices (IDDI) from FY-3/VIRR[10], and the Sentinel-5P/TROPOMI Absorptive Aerosol Index (UVAI) provided by Sentinel-5P/TROPOMI[11]. These tools have effectively enabled the quantitative analysis of the spatial and temporal distributions of dusty weather and pollution characteristics[10]. Additionally, $PM_{10,}$ as a key indicator reflecting the intensity of sand and dust, is widely used in the quantitative study of sand and dust processes. Numerical simulation is also an essential tool for studying sand and dust weather and its environmental impacts. The HYSPLIT (Hybrid Single Particle Lagrangian Integrated Trajectory) model is widely used for sand and dust traceability and transport path analysis due to its ability to accurately simulate long-range aerosol transport paths. For example, Broomandi et al. used the HYSPLIT model to identify the main sources of dust storms in Iran and validated the reliability of the transport paths using MODIS aerosol data[12].

In March 2021, northern China experienced one of the strongest dust weather events in the past decade. This dusty weather event was formed under a meteorological background characterized by high temperatures, low precipitation, and strong cyclonic activity in Mongolia[13]. However, studies on the specific impacts of this dusty weather on regional air quality and its transport paths remain relatively limited. To address this research gap, this paper comprehensively utilizes aerosol and gaseous pollutant data, including UVAI, SO_2, NO_2, and O_3, provided by Sentinel-5P/TROPOMI, as well as ground-based observation data of $PM_{2.5}$ and PM_{10}, to analyze the characteristics of air quality changes during the dusty weather. Additionally, the sources and transport paths of sand and dust are thoroughly investigated through backward trajectory simulation and cluster analysis using the HYSPLIT model. The findings of this study will provide a scientific basis for the emergency monitoring of dusty weather and the development of regional joint prevention and control policies.

2. Overview of the study area

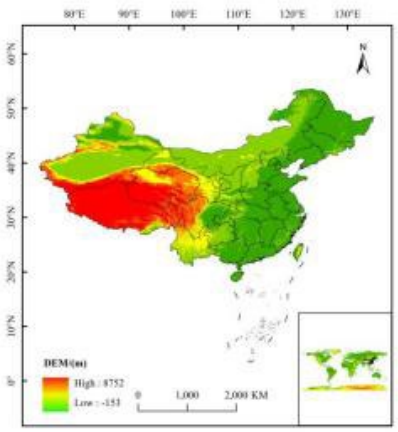

Figure 1: Overview of the research field in China

Figure 1 shows an overview map of the study area for this paper. The study area of this paper is China,

ISSN 2616-5872 Vol. 7, Issue 1: 23-36, DOI: 10.25236/AJEE.2025.070103

where sand sources are distributed in Northwest China, Inner Mongolia Autonomous Region, as well as Northeast China, North China, and North Central China, which are in the downstream area of sand transport. The latitude and longitude range from 26°N to 54°N and 74°E to 136°E. China has vast deserts and sandy soils, including the Taklamakan Desert, the Kuruktag Desert, and the Badanjilin Desert. These geographic environments provide a rich source of dust storms and form the basis for the formation and expansion of dusty weather during transport. Most dust storms in China occur in spring and fall, primarily due to specific weather systems and meteorological phenomena at these times, such as the northwest monsoon, cold waves, and cold air[14]. The northwest monsoon blows over the northern and western regions of China during spring and fall, bringing strong winds and dry climatic conditions that favor the formation of dust storms[15]. Much of China, particularly the inland and northwestern regions, is characterized by a dry climate with low relative humidity, low precipitation, and insufficient soil moisture. These climatic conditions lead to rapid evaporation of surface moisture, reduced soil retention capacity, and increased susceptibility to soil wind erosion, contributing to the occurrence of sand and dust storms[16].

3. Data and research methods

3.1. Data sources

Daily data on atmospheric ozone column densities (here tropospheric ozone column densities) in the Middle East from 2010 to 2020 provided by OMI on board the Aura satellite were used in this study. The data have a spatial resolution of 13 km × 24 km, a sensor field of view of 114°, a wavelength range of 270 to 500 nm, an average spectral resolution of 0.5 nm, and a swath width of 2,600 km. These data were downloaded from the Goddard Center for Earth Science Data and Information Services on the official website of NASA and stored in HDF5 format. Various types of meteorological data information of the study area were obtained from the National Science and Technology Resources Sharing Service Platform of the National Earth System Science Data Center of China. The DEM (Digital Elevation Model, DEM) was produced using the SRTM (Shuttle Radar Topography Mission, SRTM) Digital Terrain Elevation Model (DTEM) data package.

CHAP is a long-term, comprehensive, high-resolution, and high-quality dataset of ground-level air pollutants in China. It is generated from big data, including ground-based measurements, satellite remote sensing products, atmospheric reanalysis, and model simulations, using artificial intelligence to account for the spatial and temporal heterogeneity of air pollution. The CHAP dataset includes seven major air pollutants (PM_1, $PM_{2.5}$, PM_{10}, O_3, NO_2, SO_2, and CO), the chemical composition of $PM_{2.5}$ (SO_4^{2-}, NO^{3-}, NH^{4+}, C^{l-}, BC, and OM), and ambient polycyclic aromatic hydrocarbons (PAH_s), including seven carcinogenic PAHs (BaA, Chr, BbF, BkF, BaP, DahA, and IcdP). The study utilized ground-based surface monitoring data from the China High-Resolution High-Quality Near-Surface Air Pollutants Dataset [17]

3.2. Research methodology

It is a statistical analysis method based on atmospheric trajectory data, aimed at grouping and clustering a large number of similar trajectories to identify major air mass transport paths, pollutant source locations, and transport patterns. This method is commonly used for long-distance transport analysis of air pollution, dust storms, volcanic ash, and other substances.

Potential Source Contribution Factor (PSCF) is a statistical analysis method commonly used in environmental sciences to determine the potential source regions of pollutants and their contributions. The basic principle of the PSCF method is to integrate atmospheric pollutant concentrations with meteorological trajectory data to identify the probable source regions of the pollutants through trajectory analysis.

4. Results and analysis

China's air quality is represented by six environmental elements, such as PM_{10}, $PM_{2.5}$, NO_2, SO_2, CO, and O_3. For the convenience of mapping and viewing the spatial and temporal distributions, in this paper, PM_{10} and $PM_{2.5}$ are analyzed with ground-based monitoring data, while SO_2, NO_2, O_3, and UVAI are analyzed based on remote sensing data.

ISSN 2616-5872 Vol. 7, Issue 1: 23-36, DOI: 10.25236/AJEE.2025.070103

4.1. Ground data results and analysis

4.1.1. PM10 characterization

According to the Ambient Air Quality Standards (GB 3095-2012), PM_{10} is categorized into six classes: Class I (0 μg/m³ to 75 μg/m³), Class II (76 μg/m³ to 150 μg/m³), Class III (151 μg/m³ to 250 μg/m³), Class IV (251 μg/m³ to 350 μg/m³), Class V (351 μg/m³ to 420 μg/m³), and Class VI (421 μg/m³ to 4943 μg/m³). Figure 2 illustrates the temporal and spatial distributions of PM_{10} over a 26-day period from March 10 to April 1, 2021. Based on this distribution, it can be determined that a total of two dust storms occurred.

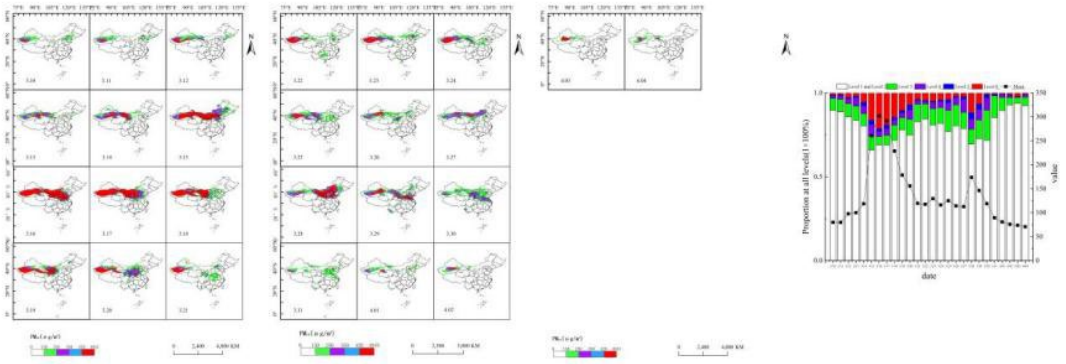

Figure 2: Spatial distribution of PM10 in dusty weather and changes in percentage and mean value of different classes

According to Figure 2, the first dust storm occurred from March 12 to 19. During this period, PM_{10} pollution spread from west to east, gradually expanding from Xinjiang to Heilongjiang via Inner Mongolia. Prior to the sandstorm, the high-value area was concentrated in the Taklamakan Desert region. Starting from March 12, PM_{10} concentrations increased rapidly, and the high-value zone expanded significantly. On March 16, the area of Grade 6 pollution reached its maximum, covering Xinjiang, Gansu, Inner Mongolia, Ningxia, Shaanxi, and extending eastward to Shenyang, Jilin, and Heilongjiang, and southward to Hebei, Beijing, Tianjin, Shandong, and other areas. The Grade 6 polluted area covered 21.17% of the country's area, a 27-fold increase from March 10. On March 16, PM_{10} concentrations peaked at 4943.6 μg/m³, with an average concentration of 302.1μg/m³, representing increases of 468.53% and 377.51%, respectively, compared to pre-dust storm levels. From March 17 to 20, the pollution area stopped expanding and began to gradually contract, with PM_{10} concentrations declining. By March 21, the first sandstorm was essentially over.From March 22 to 26, the area entered a transition period, with the Grade 6 polluted area mainly concentrated in Xinjiang, covering 4-5% of the national area, a 4-5 fold increase from before the sandstorm. The second dust storm began on March 27, with high PM_{10} concentrations spreading from central Inner Mongolia, showing a fan-like pattern from north to south. By March 28, the Grade 6 polluted area was primarily concentrated in North China, covering 11.64% of the country's area, a 12-fold increase from pre-dust storm levels. On March 28, the highest PM_{10} concentration reached 2496.9 μg/m³, with an average concentration of 173.9 μg/m³, representing increases of 236.68% and 216.25%, respectively, compared to pre-dust storm levels. From March 29, the pollution area gradually narrowed, and by March 31, the second dust storm was essentially over. By April 1, the pollution range and PM_{10} concentrations had largely returned to pre-dust storm levels, marking the end of the dust storm.

During this dust storm, PM_{10} pollution exhibited two distinct phases of outbreak, diffusion, and contraction. The first dust storm (March 12-21) was characterized by west-to-east diffusion, with widespread coverage and high concentrations. The second dust storm (March 27-31) was marked by north-to-south diffusion, affecting a smaller but still significant area. Both the area of Level 6 pollution and PM_{10} concentrations increased substantially during the dust storms, highlighting the substantial impact of intense dusty weather on regional air pollution.2.2

4.1.2. PM2.5 characterization

Figure 3 shows the spatial distribution of $PM_{2.5}$ from March 10 to April 4. According to the "Ambient Air Quality Standards" (GB 3095-2012), $PM_{2.5}$ is divided into six classes: Class I (0 μg/m³ to 35 μg/m³), Class II (36 μg/m³ to 75 μg/m³), Class III (76 μg/m³ to 115 μg/m³), Class IV (116 μg/m³ to 150 μg/m³), Class V (151 μg/m³ to 250 μg/m³), and Class VI (251 μg/m³ to 1,155 μg/m³). As shown in the figure, the high-value area from March 10 to 11 was mainly concentrated in the South Xinjiang Basin, primarily in

ISSN 2616-5872 Vol. 7, Issue 1: 23-36, DOI: 10.25236/AJEE.2025.070103

Class IV, with the highest $PM_{2.5}$ concentration reaching 312 μg/m³. The northern part of China was mostly in Class II, with a small part in Class III, having $PM_{2.5}$ concentrations ranging from 92 μg/m³ to 154 μg/m³. Central to southern China were generally in Class I or better.From March 12 to 16, $PM_{2.5}$ pollution diffused from west to east, continuing to spread from southern Xinjiang. The pollution range continued to expand, and the Class V pollution area increased dramatically on March 15, growing by approximately 477.7% compared to before the dust storm, which was about 7.8 times higher. By March 16, the polluted area reached its maximum, indicating that the first sand and dust storm had affected the largest area. High-value areas were mainly in Xinjiang, Inner Mongolia, Gansu, Qinghai, Ningxia, Shaanxi, Shanxi, Hebei, Henan, northern Anhui, Hubei, and Hunan, with the maximum concentration peaking at 1,155.70 μg/m³. Compared to the beginning of the dust storm, the daily average concentration increased from 46.34 μg/m³ on March 14 to 78.63 μg/m³ on March 16, a 69.68% increase.From March 17, the pollution range stopped expanding and began to show a gentle decline. By March 21, the large-scale pollution in the country had largely disappeared, with only a small area of pollution remaining in the Taklamakan region, marking the end of the first sandstorm. From March 22 to 26, the pollution range and high-value areas remained relatively stable.From March 27 to 28, the second dust storm originated from central Inner Mongolia and spread fan-shaped to the southern region. The maximum concentration reached 435 μg/m³, a 33.4% increase from the beginning of the dust storm, with the daily average concentration being 48.68 μg/m³, showing no significant change. After March 29, the pollution area began to contract, and by April 4, $PM_{2.5}$ pollution had largely disappeared.

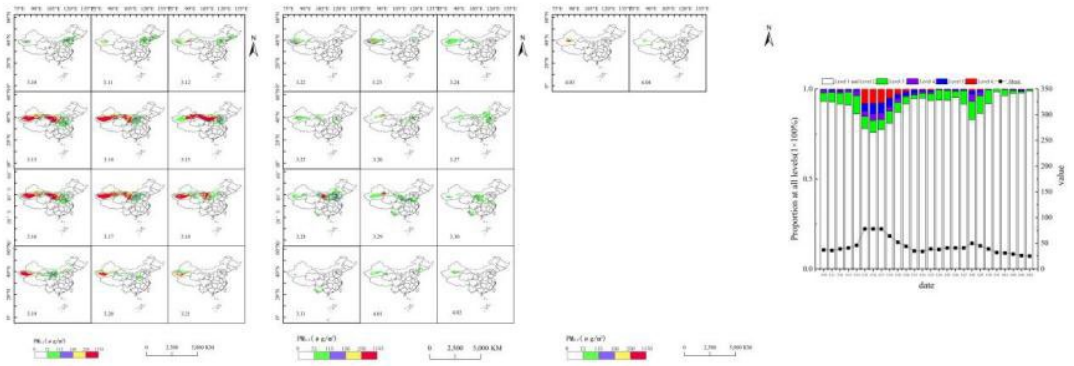

Figure 3: Spatial distribution of PM2.5 in dusty weather and changes in percentage and mean value of different classes

The spatial and temporal changes in $PM_{2.5}$ are generally consistent with those of PM_{10}, although the pollution area is smaller and the concentration changes are less pronounced, indicating that PM_{10} pollution is more severe than $PM_{2.5}$ during sandstorms.

4.2. Remote sensing data results and analysis

In the process of studying the remote sensing data, the following nine phases were defined to analyze the distribution and changes of UVAI, SO_2, NO_2, and O_3 pollutants: (1) The first three days of the dusty weather (March 10-12) (Stage 1).(2) The first dust storm outbreak period (March 13-15) (Stage 2).(3)The first dust storm decay period (March 16-18) (Stage 3).(4)The first dust storm end period (March 19-21) (Stage 4).(5) The transition period (March 23-26) (Stage 5).(6) The second dust storm outbreak period (March 27-28) (Stage 6).(7) The second dust storm decay period (March 29-31) (Stage 7).(8) The second dust storm end period (April 1-3) (Stage 8).(10) Three days after the end of the dusty weather (April 4-6) (Stage 9).

4.2.1. UVAI characterization

As shown in Figure 4, during Stage 1 (pre-dust storm period), UVAI was higher in the northwest and northeast regions and lower in the southwest and northern China. High-value areas were concentrated in the northwest and northeast, while the southwest and northern regions had low and medium concentrations. In Stage 2 (first dust storm outbreak), the median UVAI range expanded significantly, showing a clear west-to-east trend. In Stage 3 (first dust storm attenuation), large high UVAI areas appeared in Xinjiang, Inner Mongolia, and Gansu, with the maximum concentration increasing from 2.19 to 3.69, a 189% increase. In Stage 4 (end of the first dust storm), the high-value area narrowed, and the maximum value decreased slightly. However, the mean UVAI value peaked from 0.57 to 0.94, a 64% increase, and the minimum value also increased, indicating an expansion of low and medium-value

ISSN 2616-5872 Vol. 7, Issue 1: 23-36, DOI: 10.25236/AJEE.2025.070103

pollution zones. In Stage 5 (transitional period), high-value UVAI areas were mainly in Xinjiang, and the overall concentration decreased. From Stage 6 to Stage 7 (second dust storm outbreak and later stages), the contaminated area spread from north to south, expanding to Heilongjiang in the north and Guangdong in the south, with a significant increase in coverage. By Stage 8 (end of the second dust storm), pollution in the northern region largely disappeared, and high-value areas were concentrated in Guizhou, Hunan, and Guangdong. The maximum UVAI concentration increased from 2.64 to 3.77, a 193% increase. At this time, the mean and minimum UVAI values showed a gentle decline. In Stage 9 (late stage of the dusty weather), UVAI pollution largely disappeared, and the distribution became uniform. Overall, UVAI changes are consistent with the temporal evolution of dust storms, but its influence range is larger than PM_{10}, suggesting that UVAI is affected by more complex transport and diffusion mechanisms during dust storms, beyond local particulate matter deposition.

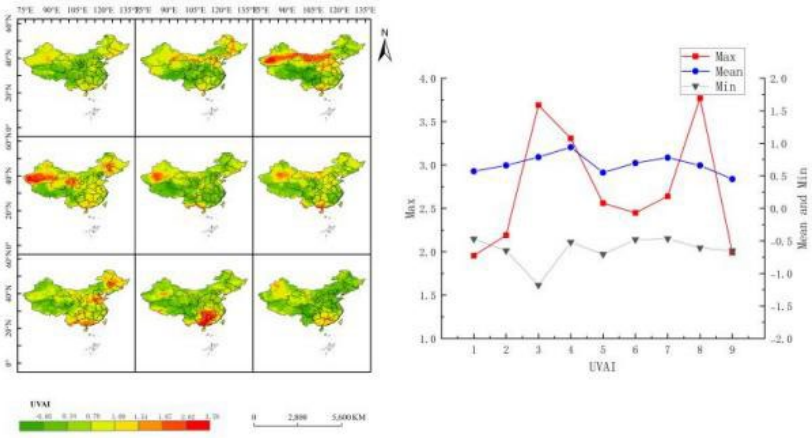

Figure 4: Spatial distribution of UVAI and variation of three values in different stages of dusty weather

4.2.2. NO_2 characterization

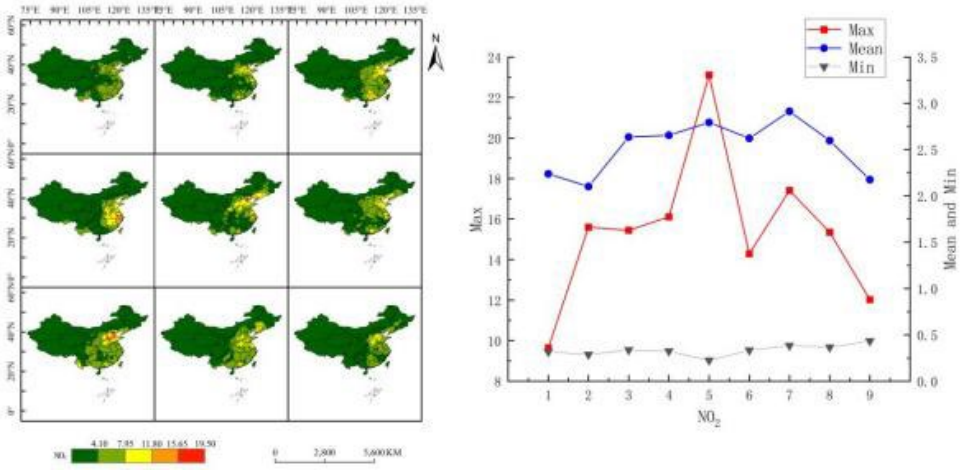

Figure 5: Spatial distribution of NO_2 and variation of three values in different stages of dusty weather

According to Fig. 5, which shows the spatial distribution and concentration changes of NO_2 during dusty weather, the response pattern of NO_2 during dust storms exhibited significant differentiation. Generally, NO_2 concentrations are low in the northwest and high in the southeast. Before the dust storm (Stage 1), high NO_2 values were concentrated in northern North China, particularly in Beijing, Tianjin, and northern Shandong, with a maximum concentration of 9.64×10^{15} molec/cm². However, the distribution was unstable. Unlike PM_{10}, which increased rapidly at the start of the sandstorm, NO_2 concentrations increased gradually. In Stage 2 (the first sandstorm outbreak), high NO_2 concentrations spread from Beijing and Tianjin to Shandong and Zhejiang, with the maximum concentration increasing by 77% compared to pre-sandstorm levels. From Stage 2 to Stage 4 (outbreak to end of the first sandstorm), the maximum NO_2 concentration remained relatively stable, indicating its distribution during the sandstorm. In Stage 7 (late stage of the second dust storm), NO_2 concentrations peaked at 23.17 ×

ISSN 2616-5872 Vol. 7, Issue 1: 23-36, DOI: 10.25236/AJEE.2025.070103

10^{15} molec/cm²,155% increase from pre-sandstorm levels. At this time, NO_2 concentrations in North China also increased significantly, showing a noticeable lag in the NO_2 response. Additionally, a high NO_2 concentration area formed in northern China, indicating significant impact from high NO_2 levels in the late stage of the dust storm. This suggests that NO_2 distribution and changes during dust storms are influenced by local emissions and complex factors like transport, chemical reactions, and particulate matter adsorption. In Stages 8-9 (end and late stages of the dusty weather), NO_2 concentrations did not show significant changes.

4.2.3. SO_2 characterization

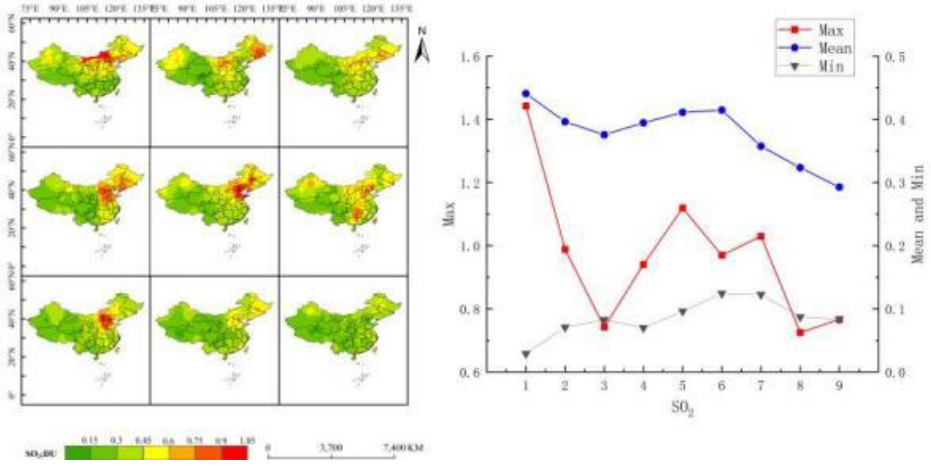

Figure 6: Spatial distribution of SO_2 and variation of three values in different stages of dusty weather

From Fig. 6, it can be seen that the high-value area of SO_2 pollution changed significantly before the onset of the sand and dust weather. In Stage 1 (pre-sand and dust storm), a large high-value area had already appeared in central Inner Mongolia, Hebei, and Beijing, with the maximum concentration and mean value reaching 1.44×10^{15} molec/cm² and 0.44×10^{15} molec/cm², respectively, both peak values.In Stages 2-3 (during the first dust storm), the high-value area gradually narrowed, and the maximum SO_2 concentration decreased sharply from 1.44×10^{15} molec/cm² to 0.74×10^{15} molec/cm², a 48.6% decrease; the mean value also decreased to 0.37×10^{15} molec/cm², a 18.7% decrease. This suggests that SO_2 is rapidly diluted at the beginning of the dust storm due to enhanced boundary layer turbulence caused by high wind speeds, which increases atmospheric mixing and diffusion, leading to a significant reduction in concentration[18].By Stages 4-5 (end of the first sandstorm and the transition period), the polluted area in Northeast and North China expanded again, with high-value areas mainly concentrated in Beijing and North China. The maximum and mean SO_2 concentrations recovered but did not return to pre-sandstorm levels. In Stage 6 (the second dust storm outbreak), the medium and high-value areas gradually weakened from north to south. In Stage 7 (late stage of the second sandstorm), the high-value area reappeared, mainly in Hebei and Beijing. By Stages 8-9 (end and late stages of the sandstorm), the polluted area largely disappeared.

Overall, the maximum and mean SO_2 concentrations showed an overall decreasing trend, while the minimum values increased slowly. This study also found that the significant decrease in SO_2 concentration was most notable at the beginning of the dust storm. Combined with the temporal and spatial variations of PM_{10} and $PM_{2.5}$, the changes in SO_2 typically precede those of PM_{10} and $PM_{2.5}$, occurring 1-3 days earlier.

4.2.4. O_3 characterization

Figure 7 reveals the complex relationship between changes in ozone (O_3) concentration during dusty weather. O_3 concentrations decreased from north to south, and the maximum O_3 concentration showed a "hexagonal" trend, with the mean concentration exhibiting a gentle wave and the minimum value remaining largely unchanged. This indicates that the impact of dusty weather on O_3 is concentrated in specific areas. In Stages 1-3, O_3 levels were relatively stable, with a mean value of about 0.15 mol/m³ and a maximum value of about 0.21 mol/m³, and little change in the distribution of high-value areas. Between Stages 3 and 4, there was a significant increase in O_3 concentration, with the maximum value rising by 14% from 0.21 mol/m³ to 0.25 mol/m³, and the mean concentration also increasing slightly. The high-value areas were mainly in the middle and eastern parts of Inner Mongolia, Liaoning, Jilin, and Heilongjiang. In Stage 5, the maximum concentration peaked at 0.25 mol/m³. In Stages 7-9, the high-

ISSN 2616-5872 Vol. 7, Issue 1: 23-36, DOI: 10.25236/AJEE.2025.070103

value area gradually decreased, and the distribution returned to pre-dust conditions. The observed lag in O_3 response to changes is about 3-6 days, which can be attributed to the effect of dust storms on solar radiation. The initial phase of dust storms may reduce solar radiation penetration due to increased atmospheric particulate matter[19], thereby suppressing photochemical O_3 production[20]. As the intensity of the dust storm decreased, atmospheric transparency increased, leading to enhanced solar radiation and a subsequent surge in O_3 formation, peaking at Stage 5.

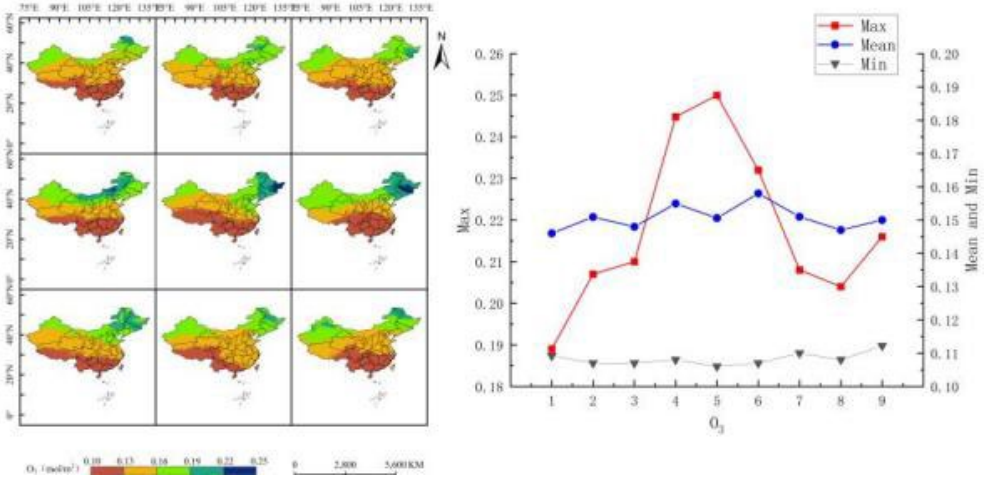

Figure 7: Spatial distribution of O_3 and variation of three values in different stages of dusty weather

5. Transmission Path and Potential Source Analysis

5.1. Transmission Path Analysis

Figure 8 shows the backward trajectory on March 19th. According to the PM_{10} distribution map, two dates, March 19 and March 31, 2021 (Beijing time), were selected for analysis. The study sites were established in the central area of the high PM_{10} concentration zone. On March 19, the sites were located at 82.6E, 40.1N (point a), 98.112E, 39.48N (point b), and 115.13E, 41.08N (point c), arranged from west to east. On March 31, the sites were situated at 86.8E, 41.45N (point d) and 114.93E, 36.35N (point e). A 72-hour backward air mass trajectory simulation was conducted for each site. For the air mass trajectory simulations, an altitude of 1000 meters was chosen, representing the upper limit of the boundary layer. Due to the significant variability of air masses at this altitude, all trajectories at 1000 meters were clustered into four primary transport pathways, which are the main airflow channels responsible for this dusty weather event.

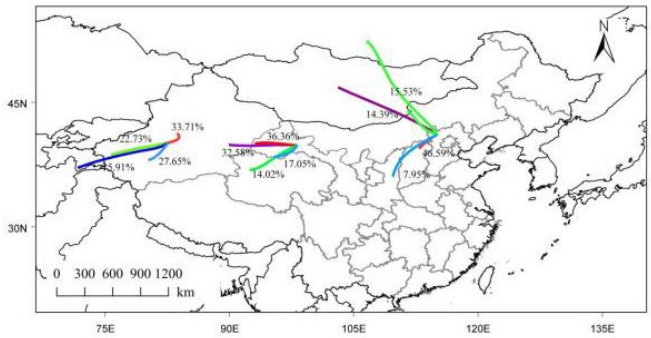

Figure 8: Backward trajectory chart for March 19

During the heavily polluted weather period from March 12 to 19, 2021, a 72-hour backward trajectory analysis revealed that the main sources of pollutants included inputs from outside the country, the Taklamakan Desert, the Gurbantunggut Desert, and the Gobi Desert in Mongolia. The air mass exhibited clear west-to-east diffusion characteristics, affecting a wide area. Specifically:

At point a, the dust air masses mainly originate from southern Kazakhstan and Kyrgyzstan and pass

ISSN 2616-5872 Vol. 7, Issue 1: 23-36, DOI: 10.25236/AJEE.2025.070103

through the Taklamakan Desert during transport. Trajectory 1 has the highest share (50.38%), followed by trajectory 2 (32.58%). Both trajectories have long transmission distances and accumulate a large amount of sand and dust while passing through the Taklamakan Desert, significantly increasing the pollutant concentration. Additionally, trajectory 4 (6.44%), despite having the shortest transmission distance, comes directly from the arid Gurbantunggut Desert and carries a substantial amount of sand and dust, contributing significantly to localized pollution.At point b, the main sources of pollutants are dominated by inputs from the Western Desert and Mongolia. Trajectory 1 (33.33%) originates from the Taklamakan Desert and passes through northern Qinghai, trajectory 2 (28.03%) is directly transported from the Gurbantunggut Desert to point b, and trajectory 3 (25.00%), despite the shorter transmission distance, carries a large amount of sand and dust due to its origin in the eastern Taklamakan Desert. Trajectory 4 (originating from the Siberian Plain of Russia) enters Gansu through Mongolia, then sharply turns and finally arrives at point b, showing the pollution characteristics of the western desert superimposed on the inputs from outside the country.At point c, the air mass is mainly transported from the Russian Siberian Plain and the Mongolian Gobi Desert. Trajectory 1 (39.39%) arrives at point c after passing through the Gobi Desert of Mongolia, which is the main reason for the significant increase in PM_{10} values. Trajectory 2 (37.50%) is transported from the Gobi Desert of Mongolia to the north of Shanxi Province, and is deflected after being influenced by a west-to-east air mass, directly entering point c. Trajectories 3 and 4, accounting for 12.88% and 10.23% respectively, pass through Mongolia and contribute a smaller but not negligible portion of the pollution at point c.

Overall, the main pollutant input paths for this heavily polluted weather included Kazakhstan, southern Kyrgyzstan, the Taklamakan Desert, the Gurbantunggut Desert, the Gobi Desert in Mongolia, and the Siberian Plain in Russia. The west-to-east transport of air masses through the Taklamakan and Gurbantunggut Deserts accumulated large concentrations of dust and sand, significantly exacerbating air pollution in central and eastern China. Additionally, the Mongolian cyclone had a significant driving effect on air mass transport, extending the sand and dust pollution to these regions. The input from Mongolia gradually increased its contribution to regional pollutant concentrations. These compounding effects of foreign sand and dust inputs and local deserts led to a significant increase in PM_{10} concentration and the rapid expansion of the pollution range during this heavily polluted weather.

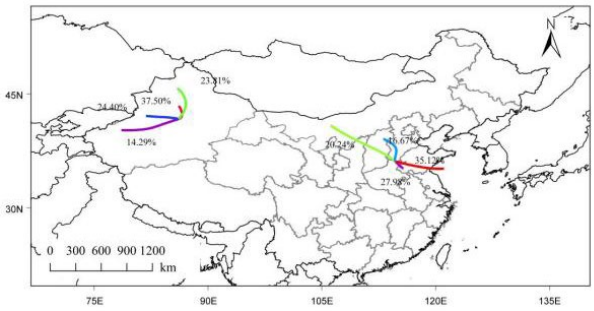

Figure 9: Backward trajectory chart for March 31

Figure 9 shows the backward trajectory on March 31.During the period of heavy pollution weather from March 28 to March 30, 2021, a 72-hour backward trajectory analysis reveals that the major pollutant transport paths at points d and e exhibit significant foreign input and regional desert contributions, while being significantly influenced by the Mongolian cyclone. The details are as follows:

Analysis of Air Mass Trajectories at Point d: Trajectory 1: The main contributing path of pollution at point d. It originates from the Korla Desert, travels southeast, and then, influenced by the Mongolian air mass, undergoes a significant turn of over 90°, arriving at point d with a share of 35.42%. This significant turn indicates the strong influence of the Mongolian air mass on the airflow path.Trajectories 2 and 4: Both travel from east to west, merging in Kyrgyzstan and jointly entering the fringe region of the Taklamakan Desert in Xinjiang, contributing significantly to the pollution at point d with proportions of 26.67% and 12.08%, respectively. The fusion of these two trajectories, combined with the cumulative effect of sand and dust in the Taklamakan Desert, further increases the pollutant concentration.Trajectory 3: Originates from Kazakhstan with a longer transport path. Although influenced by the Mongolian air masses, the turning angle is less significant than that of Trajectory 1, and its contribution to the pollution at point d is relatively small.Analysis of Air Mass Trajectories at Point e:All Four Transport Corridors**: Characterized by northwest to southeast transport and show cyclonic turns under the influence of the Mongolian air mass. Trajectories 2 and 3 have larger turning angles, indicating the strong influence of the Mongolian air mass on the paths of the air masses.Trajectories 1 and 4: Have longer transmission

ISSN 2616-5872 Vol. 7, Issue 1: 23-36, DOI: 10.25236/AJEE.2025.070103

paths, both originating from outside the country. During transmission, these two trajectories intersect in the Sayanling area and continue to transport to point e, showing the superposition effect of regional and cross-border transport.Trajectory 2: Has the shortest transport distance, accounting for 32.92% of the total, and originates from the Maowusu Desert in central Inner Mongolia, carrying a large amount of sand and dust. This trajectory is the main contributing path to the increase in PM_{10} values at point e. The sand and dust transport from the Maowusu Desert highlights the significant influence of regional desert sources on pollution.During the sand and dust storms from March 13 to March 31, the high PM_{10} values in Northwest China were mainly contributed by transport paths from outside the country, which passed through the Taklamakan Desert and the Gurbantunggut Desert under the influence of the Mongolian air mass, carrying a large amount of sand and dust, which significantly increased the regional pollution concentration; whereas the elevated PM_{10} in North China was mainly contributed by the input paths from Mongolia and the Maowusu Desert under the effect of Mongolian air mass sand and dust transportation. This suggests that the compound effect of foreign inputs and regional desert sources is the key factor leading to the rise of PM_{10}, while the strong influence of the Mongolian air mass exacerbates the scope and intensity of pollutant transport.

5.2. Potential source analysis

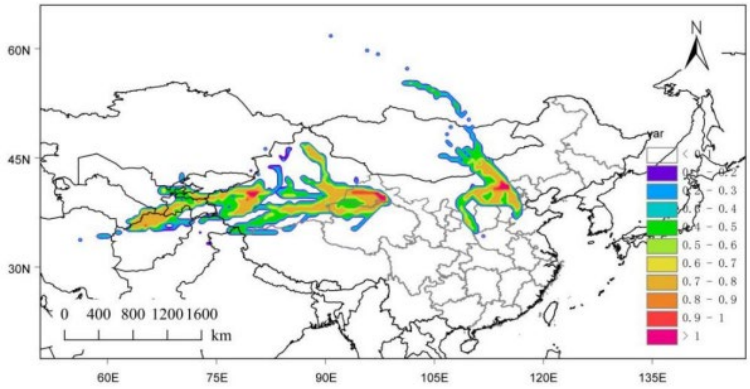

Figure 10: Map of potential sources of dust storms from March 13 to 19

Analyze the location of the center of the PM_{10} high-value area. From Fig.10, it can be seen that the PSCF at point A is mainly distributed in the southwest direction, with high-value areas concentrated in two regions: the border areas of Uzbekistan, Tajikistan, and Afghanistan, as well as the Taklamakan Desert. Low-value areas of the PSCF are relatively less distributed.At point B, PSCF high values are mainly distributed in southwest Xinjiang and the Gurbantunggut Desert, while low values are mainly distributed in the southern part of the Taklamakan Desert.At point C, PSCF high values are mainly distributed in the Maowusu Desert and part of southern Mongolia, while low values are mainly distributed in Mongolia.

Therefore, the main potential source areas of exotic aerosol transport during the dust storm from March 13 to March 18, 2021, at point A are the Karakum Desert and the Registan Desert, as well as the Taklamakan Desert. At point B, the main potential source areas are the Taklamakan Desert and the Gurbantunggut Desert. At point C, the main potential source areas are the Maowusu Desert and the Gobi Desert in Mongolia.

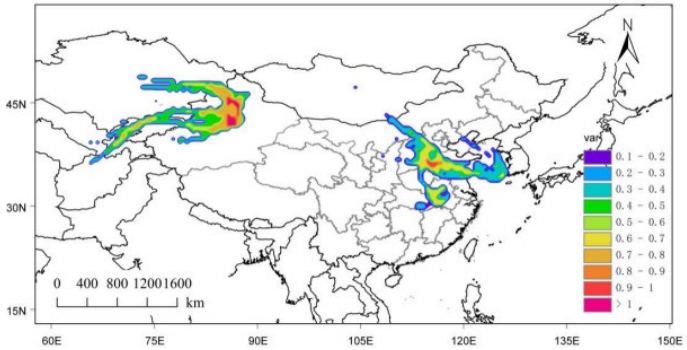

Figure 11: Potential Source Distribution of Dust Storms from March 27 to 31

ISSN 2616-5872 Vol. 7, Issue 1: 23-36, DOI: 10.25236/AJEE.2025.070103

Figure 11 shows the characteristics of the regional distribution of high PSCF (Potential Source Contribution Factor) values at point D. It can be seen that the high-value region at point D is primarily concentrated in the Gurbantunggut Desert, while the low-value region extends to the west. At point E, the high PSCF values across Kyrgyzstan are mainly distributed in the northwestern and southeastern directions. Combined with the backward distribution analysis, the pre-distribution of point E is significantly influenced by atmospheric stability. This distribution feature is related to the transport path of the Mongolian air mass from the northwest to the southeast, where a cyclonic turn occurs, causing a backward flow in the southeastern periphery. This results in the current PSCF distribution at point E. It can be seen that the main potential sources at point D are the Gurbantunggut Desert, the Karakum Desert, and the Aral Sea region, while the main potential source at point E is the Mongolian Gobi Desert.

By analyzing the location of the centers of the two PM_{10} high-value areas using the PSCF method of potential source area contribution factor analysis, it can be seen that the two dust transports to China exhibit similar characteristics, moving from west to east. The potential source areas of dust from west to east undergo regular changes. The potential source areas in Northwest China are primarily the Taklamakan Desert and the Gurbantunggut Desert in Xinjiang, while the foreign potential sources are mainly the border areas of Uzbekistan, Tajikistan, Afghanistan, and the Kazakh Hills. Dust transport from Mongolia increases as it moves from west to east, entering North China and further extending to Central China. The foreign dust sources in North China are mainly the Sayan Ridge and the southern Gobi Desert of Mongolia. Through the south, the dust passes through the Badanjilin Desert, the Yamalayk Desert, the Ulan Buh Desert, the Qubuqi Desert, and the Hunsandak Sands. The main transmission corridors are the northeastern and northwestern routes. The domestic dust sources in the west of North China are primarily the Kumtagh Desert, the Taklamakan Desert, and the Gurbantunggut Desert. Central North China's dust transport is mainly in the northwest direction, originating from the southern Gobi Desert of Mongolia. The domestic dust sources have a greater impact, primarily from the Tengger Desert in Inner Mongolia.

6. Conclusions

The dusty weather in mid-March 2021 was characterized by its long duration, wide range, and high intensity. In this study, satellite data and PM_{10} and $PM_{2.5}$ data were combined to dynamically monitor the dust weather process in the horizontal direction. The sources and transport paths of the dust were analyzed using HYSPLIT backward trajectory clustering. Simultaneously, the regional distribution changes of four pollutants—UVAI, SO_2, NO_2, and O_3—in terms of their ranges and concentrations during the dust storm were analyzed, leading to the following main conclusions:

(1) Two consecutive strong dust storms occurred between March 13 and March 30, 2021. Both $PM_{2.5}$ and PM_{10} exhibited overall west-to-east distribution changes, with a wide range of influence. During the first sandstorm, $PM_{2.5}$ and PM_{10} pollution peaked on March 16, with concentrations of 1155.7 μg/m³ and 4943.3 μg/m³, respectively, which were 468.53% higher than those before the sandstorm. The pollution covered northwestern regions such as Xinjiang, Inner Mongolia, Gansu, Ningxia, and Shaanxi, and gradually extended to northern and northeastern China and parts of eastern China. The impact range of the second sandstorm reached its maximum on March 28, with peak $PM_{2.5}$ and PM_{10} concentrations of 435.6 μg/m³ and 1,589.11 μg/m³, respectively, covering North China and parts of Central and Eastern China. Compared with the daily mean concentrations before the dusty weather, PM_{10} increased by 127.1% and $PM_{2.5}$ by 77.1% during the first sandstorm, while PM_{10} increased by 42.5% and $PM_{2.5}$ by 48.5% during the second sandstorm. Overall, PM_{10} pollution levels were significantly higher than $PM_{2.5}$ during both sandstorms, reflecting the significant impact of strong dusty weather on regional air pollution and the extremely wide range of impacts.

(2) Dust and sandstorms have significant and diverse impacts on China's atmospheric environment, and different atmospheric components exhibit unique spatial and temporal evolutionary characteristics. The spreading range of UVAI is generally consistent with the evolution of dust and sandstorms, and its impact range is much larger than that of PM_{10}, suggesting that UVAI is influenced by complex transport and diffusion mechanisms. The maximum peak concentration of UVAI is 3.69, which is 189% higher than the pre-dust and sandstorm period. The mean peak value is 0.94, an increase of about 64%.The response of NO_2 shows a noticeable lag, with concentrations exhibiting a distribution pattern of low in the northwest and high in the southeast, influenced by the combination of complex transport, chemical reactions, and particle adsorption. The peak concentration of NO_2 is 23.17×10^{15} molec/cm², and the mean peak value is 2.91×10^{15} molec/cm², representing increases of 155% and 24%, respectively, compared to the pre-dust storm period.SO_2 concentrations show an overall downward trend, with a

ISSN 2616-5872 Vol. 7, Issue 1: 23-36, DOI: 10.25236/AJEE.2025.070103

significant decrease at the beginning of the dust storm due to enhanced turbulence. The maximum value decreases from a peak of 1.44×10^{15} molec/cm² to 0.74×10^{15} molec/cm², a reduction of about 94.6%. This change occurs earlier than that of PM_{10} and $PM_{2.5}$, indicating a strong influence of atmospheric turbulence at the onset of the dust storm.O_3 concentrations exhibit a decreasing trend from north to south. In the late stage of the dust storm, due to increased atmospheric transparency and enhanced solar radiation, O_3 concentrations show a dramatic increase. The maximum value and mean peak concentration reach 0.25 mol/m³ and 0.15 mol/m³, respectively, with the mean concentration increasing by about 32%. This response lags behind the intensity of the sandstorm, and some areas experience a delayed impact.In summary, dust storms not only directly affect particulate matter concentrations but also significantly alter the spatial and temporal distribution and concentration changes of other atmospheric components such as UVAI, NO_2, SO_2, and O_3 through complex physical and chemical processes, revealing the multiple impact mechanisms of dust storms on the atmospheric environment.

(3) The sand source of this dust storm is complex, and the transmission path is mainly divided into three branches: the northwest route, the west route, and the north route. The first dust storm primarily originates from Kazakhstan, southern Kyrgyzstan, and the western part of the basin, transmitting to China through the Taklamakan Desert in Xinjiang and the Gurbantunggut Desert, continuing to the eastern part. During the transmission process, it becomes the main source of sand and dust weather in northern China on March 14 and 15. Central Mongolia and central-western Inner Mongolia contributed significantly to the sand and dust on March 16 to 18, affecting 20 provinces and cities in China and the near-shore sea area of the Bohai Sea. Overseas dust sources were mainly the Korla Desert and the Gobi Desert in southern Mongolia. Domestic dust sources were primarily the Taklamakan Desert, Gurbantunggut Desert, Mao Wusu Desert, and Tengger Desert.

Acknowledgement

Statements and Declarations

Funding This work was funded by Lanzhou Science and Technology Plan Project(2017-RC-69)and the National Natural Science Foundation of China (2016YFC0500907) at the Key Laboratory of Resource Environment and Sustainable Development of Oasis, Gansu province,and the Gansu Province Environmental Science and Engineering Demonstration Laboratory.

Author Contributions

Jiaqi Wang: methodology, writing-original draft review and editing, data curation, resources, visualization, formal analysis.

Tianzhen Ju: project administration, conceptualization, writing-review and editing, methodology, supervision.

Bingnan Li: writing-review and editing, data curation.

Yaqun Cao:writing-review and editing,investigation, formal analysis

Jiachen Li: writing-review and editing, investigation, formal analysis. resources, data curation.

Data availability

The air pollutant data used during this study are from the NASA, and other datasets analyzed are available from the corresponding author on reasonable request.

Ethical Responsibilities of Authors

“All authors have read, understood, and have complied as applicable with the statement on "Ethical responsibilities of Authors" as found in the Instructions for Authors”.

Consent to Participate

This paper does not require consent to participate.

ISSN 2616-5872 Vol. 7, Issue 1: 23-36, DOI: 10.25236/AJEE.2025.070103

Consent for Publication

The first author and the responsible author agree to publish the paper.

Competing Interests

The authors declare no competing interests.

References

[1] H. Aghababaeian, A. Ostadtaghizadeh, A. Ardalan, A. Asgary, M. Akbary, M. S. Yekaninejad and C. Stephens, 2021. Global health impacts of dust storms: a systematic review. Environmental health insights. 15, 11786302211018390.

[2] C. I. Smith, L. C. Sweet, J. Yoder, M. R. McKain, K. Heyduk and C. Barrows, 2023. Dust storms ahead: Climate change, green energy development and endangered species in the Mojave Desert. Biological Conservation. 277, 109819.

[3] T. Bao, J. Li, I.-S. Chang, E. Jin, J. Wu and Y. Bao, 2022. The influence of ecological engineering projects on dust events: A case study in the northern China. Environmental Impact Assessment Review. 96, 106847.

[4] L. Song, X. Bi, Z. Zhang, L. Li, Q. Dai, W. Zhang, H. Li, X. Wang, D. Liang and Y. Feng, 2022. Impact of sand and dust storms on the atmospheric environment and its source in Tianjin-China. Science of The Total Environment. 825, 153980.

[5] A. Khammar, A. Khammar, M. Nouri, E. Saber, A. Miri, J. Vatani and m. maleki roveshti, 2023. Dust Storm Effect and Climatological Factors on Cardiovascular and Cerebrovascular Respiratory Diseases: A Literature Review. muq-hygiene. 12 2, 99-104.

[6] K. Klingmüller, V. A. Karydis, S. Bacer, G. L. Stenchikov and J. Lelieveld, 2020. Weaker cooling by aerosols due to dust–pollution interactions. Atmospheric Chemistry and Physics. 20 23, 15285-15295.

[7] J. F. Kok, T. Storelvmo, V. A. Karydis, A. A. Adebiyi, N. M. Mahowald, A. T. Evan, C. He and D. M. Leung, 2023. Mineral dust aerosol impacts on global climate and climate change. Nature Reviews Earth & Environment. 4 2, 71-86.

[8] J. Sun, M. Zhang and T. Liu, 2001. Spatial and temporal characteristics of dust storms in China and its surrounding regions, 1960–1999: Relations to source area and climate. Journal of Geophysical Research: Atmospheres. 106 D10, 10325-10333.

[9] K. Alam, T. Trautmann, T. Blaschke and F. Subhan, 2014. Changes in aerosol optical properties due to dust storms in the Middle East and Southwest Asia. Remote Sensing of Environment. 143, 216-227.

[10] P. Zhang, C. Wang, L. Chen, W. Bai, C. Qi and J. Qi, 2018. Current status of satellite-based dust aerosol remote sensing and some issues to be concerned. Meteorol. Mon. 44 12, 1000-0526.2018.

[11] Y. Xie, W. Zhang and J. J. Qu, 2017. Detection of Asian dust storm using MODIS measurements. Remote Sensing. 9 8, 869.

[12] P. Broomandi, B. Dabir, B. Bonakdarpour and Y. Rashidi, 2017. Identification of the sources of dust storms in the City of Ahvaz by HYSPLIT. Pollution. 3 2, 341-348.

[13] M. Tao, L. Chen, J. Wang, L. Wang, W. Wang, C. Lin, L. Gui, L. Wang, C. Yu and Y. Wang, 2022. Characterization of dust activation and their prevailing transport over East Asia based on multi-satellite observations . Atmospheric research. 265, 105886.

[14] W. Li, W. Wang, Y. Zhou, Y. Ma, D. Zhang and L. Sheng, 2018. Occurrence and reverse transport of severe dust storms associated with synoptic weather in East Asia. Atmosphere. 10 1, 4.

[15] W. Qian, X. Tang and L. Quan, 2004. Regional characteristics of dust storms in China. Atmospheric Environment. 38 29, 4895-4907.

[16] C. Opp, M. Groll, H. Abbasi and M. A. Foroushani, 2021. Causes and effects of sand and dust storms: What has past research taught us? A survey. Journal of Risk and Financial Management. 14 7, 326.

[17] J. Wei, Z. Li, A. Lyapustin, J. Wang, O. Dubovik, J. Schwartz, L. Sun, C. Li, S. Liu and T. Zhu, 2023. First close insight into global daily gapless 1 km PM2.5 pollution, variability, and health impact. Nature Communications. 14 1, 8349.

[18] B. Jayaraman and J. G. Brasseur, 2021. Transition in atmospheric boundary layer turbulence structure from neutral to convective, and large-scale rolls. Journal of Fluid Mechanics. 913, A42.

[19] P. G. Kosmopoulos, S. Kazadzis, M. Taylor, E. Athanasopoulou, O. Speyer, P. I. Raptis, E. Marinou, E. Proestakis, S. Solomos, E. Gerasopoulos, V. Amiridis, A. Bais and C. Kontoes, 2017. Dust impact on surface solar irradiance assessed with model simulations, satellite observations and ground-based

ISSN 2616-5872 Vol. 7, Issue 1: 23-36, DOI: 10.25236/AJEE.2025.070103

measurements . Atmos. Meas. Tech. 10 7, 2435-2453.
[20] R. L. McKenzie, P. J. Aucamp, A. F. Bais, L. O. Björn, M. Ilyas and S. Madronich, 2011. Ozone depletion and climate change: impacts on UV radiation. Photochemical & Photobiological Sciences. 10 2, 182-198.